Supplementary Information

Allosteric potentiation of a ligand-gated ion channel is mediated by access to a deep membrane-facing cavity

Stephanie A Heusser[a,b], Marie Lycksell[a,b], Xueqing Wang[a,b], Sarah E. McComas[a,b], Rebecca J Howard[a,b], Erik Lindahl[a,b,1]

Affiliations

[a]Department of Biochemistry and Biophysics, Stockholm University, 11419 Stockholm, Sweden; [b]Science for Life Laboratory, Stockholm University, 17165 Solna, Sweden; and [c]Swedish e-Science Research Center, KTH Royal Institute of Technology, 11428 Stockholm, Sweden

[1]To whom correspondence should be addressed. Email: erik.lindahl@scilifelab.se

This PDF file includes:

- Supplementary Materials and Methods
- Supplementary Figs. S1 to S10
- References for SI reference citations

SI MATERIALS AND METHODS

Reagents

All reagents were purchased through VWR International or Sigma-Aldrich. Constructs for novel GLIC variants were generated with commercially synthesized primers using the GeneArt site-directed mutagenesis system (Thermo Fischer, Waltham, MA). Plasmids were amplified with the HiSpeed Plasmid Purfication Midi kit (Qiagen, Hilden, Germany) and mutations were confirmed using cycle sequencing services (Eurofins Genomics, Ebersberg, Germany).

Molecular dynamics simulations

Propofol (PFL) cocrystal structures of holo GLIC WT (Met-205, PDB ID 3P50) and Trp-205 variant (PDB ID 5MVN) were used as starting structures for molecular dynamics simulations. For comparison of pore hydration levels (SI Appendix Fig. S3), apo WT structures in open (PDB ID 4HFI) and closed states (PDB ID 4NPQ) were also prepared through equilibration. Because the Trp-205 structure contained PFL molecules in only four of the five subunits, a fifth PFL molecule was superimposed by alignment with a neighboring subunit to yield a pseudosymmetric holo structure. To accommodate the major backbone adjustments expected for the Gly and Pro variants, all non-hydrogen side chain atoms were first removed from the equilibrated Trp-205 system to build Gly-205; this template was then used to build Pro-205. Apo structures were obtained by deleting PFL atoms. The Amber99sb-ildn force field (1) was used to describe the proteins, which were embedded in a 1-palmitoyl 2-oleoyl phosphatidylcholine (POPC) lipid bilayer modeled with Berger force field parameters (2, 3). Protonation states were set to pH 4.6 as previously described (4). The system was solvated in a cubic box using the TIP3P water model (5), and sodium chloride was added to bring the system to neutral charge and an ionic strength of 0.1 M. PFL parameters were generated using STaGE (6), which utilizes ACPYPE and Antechamber (7-9).

All simulations were performed with Gromacs 2016.1 (10-12). The systems were energy minimized for 100,000 steps using the steepest-descent method, with equilibration over 100 ps at a constant number of particles, volume, and temperature, and the velocity rescaling thermostat (13) set to 300 K. The holo systems were equilibrated with a constant number of particles, pressure, and temperature (NPT) for at least 45 ns, during which the position restraints on the protein were gradually released. Propofol was kept restrained during the entire equilibration. The apo systems were NPT-equilibrated for 45 ns with gradual release of restraints. These long equilibration times were used to ensure best possible relaxation of the protein. In all equilibration runs, the time step was set to 2 fs, pressure was maintained at 1bar through Berendsen pressure coupling (14), and LINCS constraint algorithms (15) were applied.

For each equilibrated system, three replicates of 1-μs unrestrained simulations were generated. Parrinello-Rahman pressure coupling (16) ensured constant pressure and, as for the equilibration runs, the LINCS constraint algorithm (15) was used. In the Met-205 and Trp-205 holo simulations PFL had no virtual-site hydrogens, restricting the time step to 3 fs. For the Gly-205 and Pro-205 holo simulations

virtual site hydrogens were added to PFL, and a 5 fs time step was used. All apo simulations used a 5 fs time step.

Analysis of molecular dynamics simulations

Gromacs was used to calculate RMSDs. For these calculations, the first frame of each trajectory was used as a reference, and RMSDs were calculated from alignments of backbone α- carbons in each subsequent frame.

For cavity volume calculations, MDpocket (17) was used to identify all cavities in a starting model for each of the systems (holo and apo forms of Met, Trp, Gly and Pro variants). Points corresponding to intrasubunit PFL pockets were then selected and tracked throughout the trajectories to yield pocket volume vs. time. Propofol molecular volume was estimated from the supplier-reported density and molar mass (Sigma-Aldrich Sweden AB, Stockholm, Sweden)

VMD (18) was used for calculating distances. Pocket depth was tracked by the shortest distance between the cavity perimeter and residue Val-242. Distance between the hydroxyl oxygen of PFL and the backbone carbonyl of Ile-202 was used to evaluate possible hydrogen bond formation.

The percentage of frames during which the measured PFL-Ile-202 distance was within a cut-off of 3.5 Å was calculated. For the other propertied vs. time, averages were calculated. Error estimates for these averages were calculated with the Gromacs gmx analysis tool using block averaging, the details of which have been described previously (19). Subunits where the function used for error estimates could not be adequately fitted to the autocorrelation function were excluded from the averages and error estimates. For the pocket volume estimates from crystal structures, the standard error of the mean ($\sigma_{\bar{x}} = \sigma/\sqrt{n}$) was calculated, the five subunits giving n=5.

Pore hydration was tracked using VMD (18). The number of waters within ±2 Å along the pore axis from the center of mass of Ile-233 (9') was counted in each frame and plotted versus time. A running average over fifty points was added to guide the eye.

Molecular docking

Docking of PFL to X-ray structures was carried out using AutoDock Vina (20), reporting the top nine clusters of binding poses in each of two search volumes, ranked by mean energy score. Ligand atoms representing PFL (PDB ID 5MUO), and protein atoms representing apo-closed (4NPQ, chains A–E) and -open (4HFI) and holo-open WT (3P50) and Trp-205 (5MVN) GLIC structures, were extracted from their respective PDB files. Side-chain positions were selected and/or completed, and hydrogens and charges added, using the Dock Prep tool in UCSF Chimera (21). To dock to the intrasubunit site, search volumes of 20 x 15 x 20 Å were placed to enclose the M1–M4 helices of a single (A) subunit of each structure, extending ~4 helical registers (~50% of the conduction pathway length) from the M2–M3 loop towards the intracellular side. To dock to the channel pore, 19 x 19 x 31 Å volumes were placed parallel to the

conduction pathway, enclosing residues Thr-226 (2') through Ile-240 (16') of each structure; resulting clusters were categorized by proximity to either residue Ser-230 (6') or Ala-237 (13').

Electrophysiology

Two-electrode voltage-clamp electrophysiology was performed as previously described (22). Briefly, nuclei of *Xenopus oocytes* were injected with 0.5–6.0 ng cDNA and stored in incubation medium for 2–7 days prior to recordings. 100-mM stock solutions of PFL in dimethylsulfoxide (DMSO) were stored at 4°C. All modulators were freshly diluted in running buffer; PFL and bromoform solutions were sonicated for 2 min prior to application.

For each mutant, EC_{10} conditions were first determined as previously described (23) and as calculated below. Modulation was measured by activating the channel in EC_{10} buffer for 2 min (referred to as the pretreatment peak), then washing out for 5 min; preapplying the drug in running buffer for 1 min, coapplying in EC_{10} buffer for 2 min (cotreatment peak), then washing out for 5 min; then activating again at EC_{10} for 2 min (posttreatment peak). To measure time dependent persistence in Fig. 3*E* and SI Appendix Fig S7*B,* 100 μM PFL in running buffer (pH 7.5) was applied for 0.5, 1, 3 or 6 min instead of the usual cotreatment. To avoid artifacts from persistent drug effects, each oocytes was discarded after a single modulation protocol.

Analysis of electrophysiology data

Each recording was collected using 4–11 oocytes from at least two frogs. To determine EC_{10} conditions (the agonist concentration producing 10% maximal response), proton concentration-dependence curves were determined by nonlinear regression fit using the equation $R = R_{max}/(1+10^{\wedge}(\log EC_{10}-C)*n_H))$ for which R is the peak response, R_{max} the maximal activation, C the proton concentration, and n_H the Hill coefficient. Acute modulation in Fig. 2*F*, S6*A–C*, and S8*A–B* represents mean % ± standard error of the mean (s.e.m.) values for $((R_{co}-R_{pre})/R_{pre})*100$, where R_{pre} is the peak response prior to drug exposure (pretreatment) and R_{co} the response in the presence of modulator (cotreatment). Persistent modulation in Fig. 3*C*,E, S6*D-E*, S7*C* and S8*C-D* represents mean % ± s.e.m. values for $((R_{post}-R_{pre})/R_{pre})*100$, where R_{post} is the response after drug washout (posttreatment). Acute inhibition in Fig. 4 represents mean % ± s.e.m. values for $((R_{co}-R_{post})/R_{post})*100$. Results were analyzed using ordinary one-way analysis of variance, with significance set to $P < 0.05$. All analyses were performed using Prism 7 for Mac (GraphPad Software, La Jolla, CA).
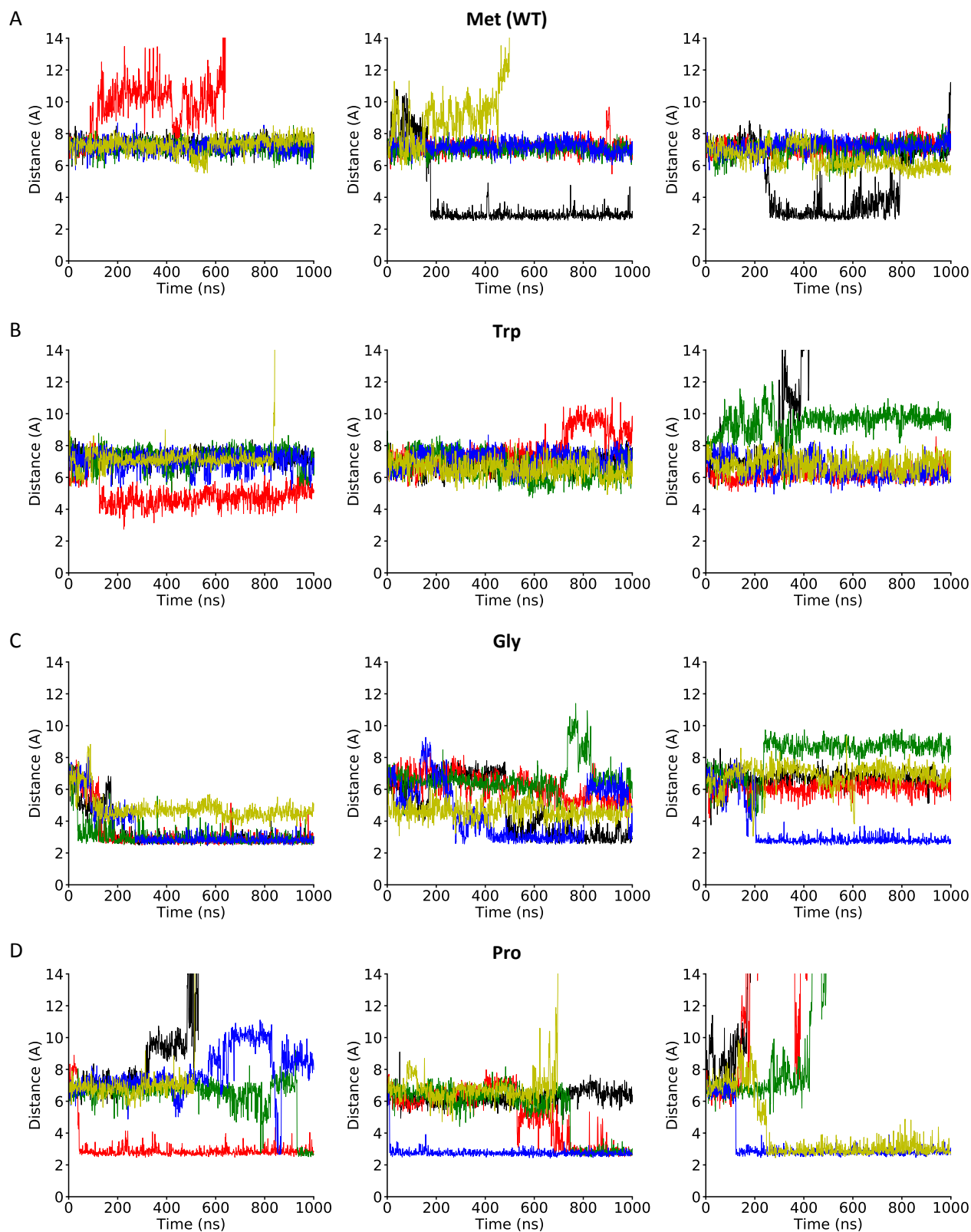
Fig. S1 Distance (y-axis, Å) between PFL and M1 residue Ile-202 over time (x-axis, ns) in each of 5 subunits (black, red, blue, green, yellow) and three replicates (*Left–Right*) for **(A)** Met-205 (WT), **(B)** Trp-205, **(C)** Gly-205 and **(D)** Pro-205 variants.
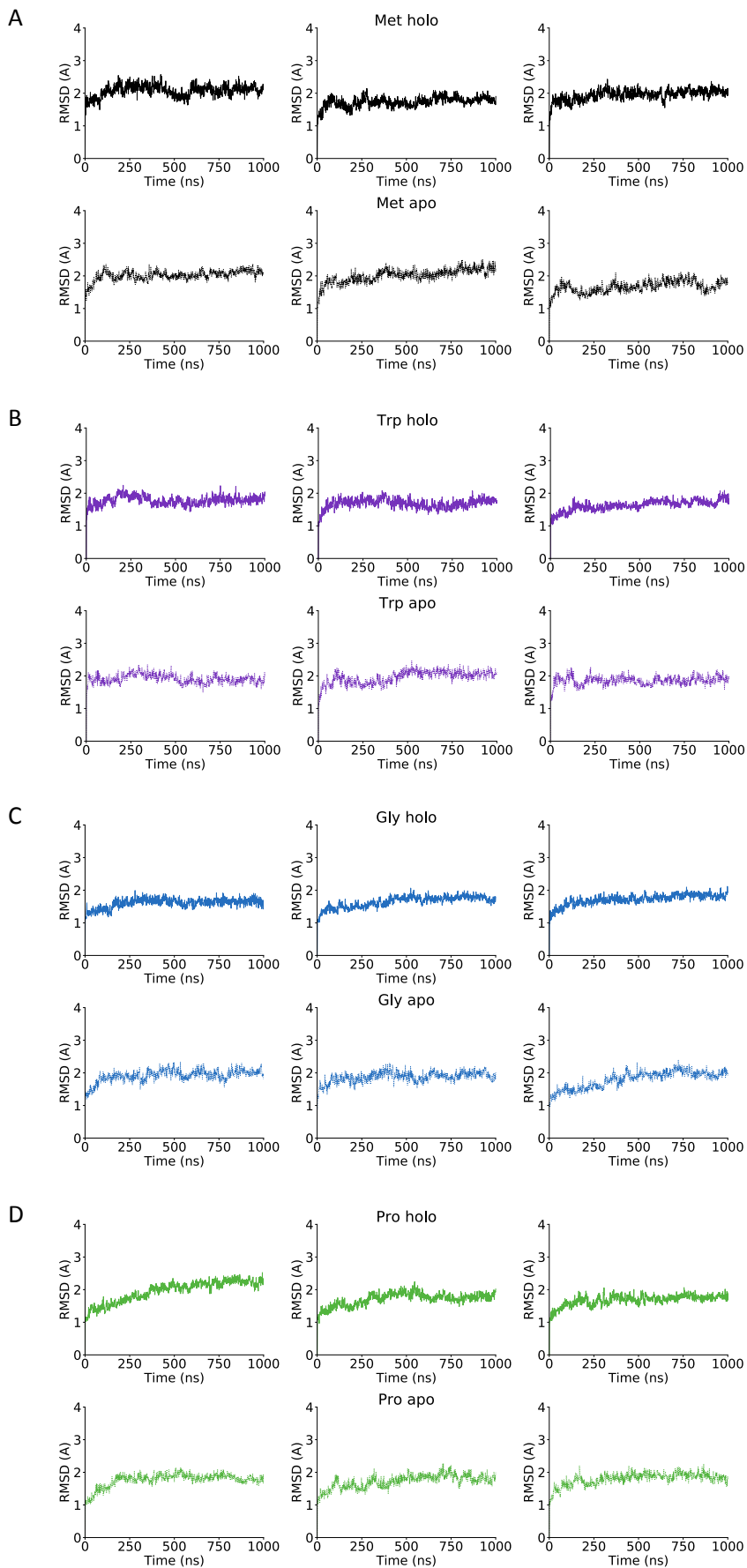
Fig. S2 C-alpha RMSDs (y-axis, Å) over time (x-axis) for holo (*Top*, ns) and apo (*Bottom*) simulations, displayed for each of three replicates for *(A)* Met-205 (WT), *(B)* Trp-205, *(C)* Gly-205 and *(D)* Pro-205 variants.
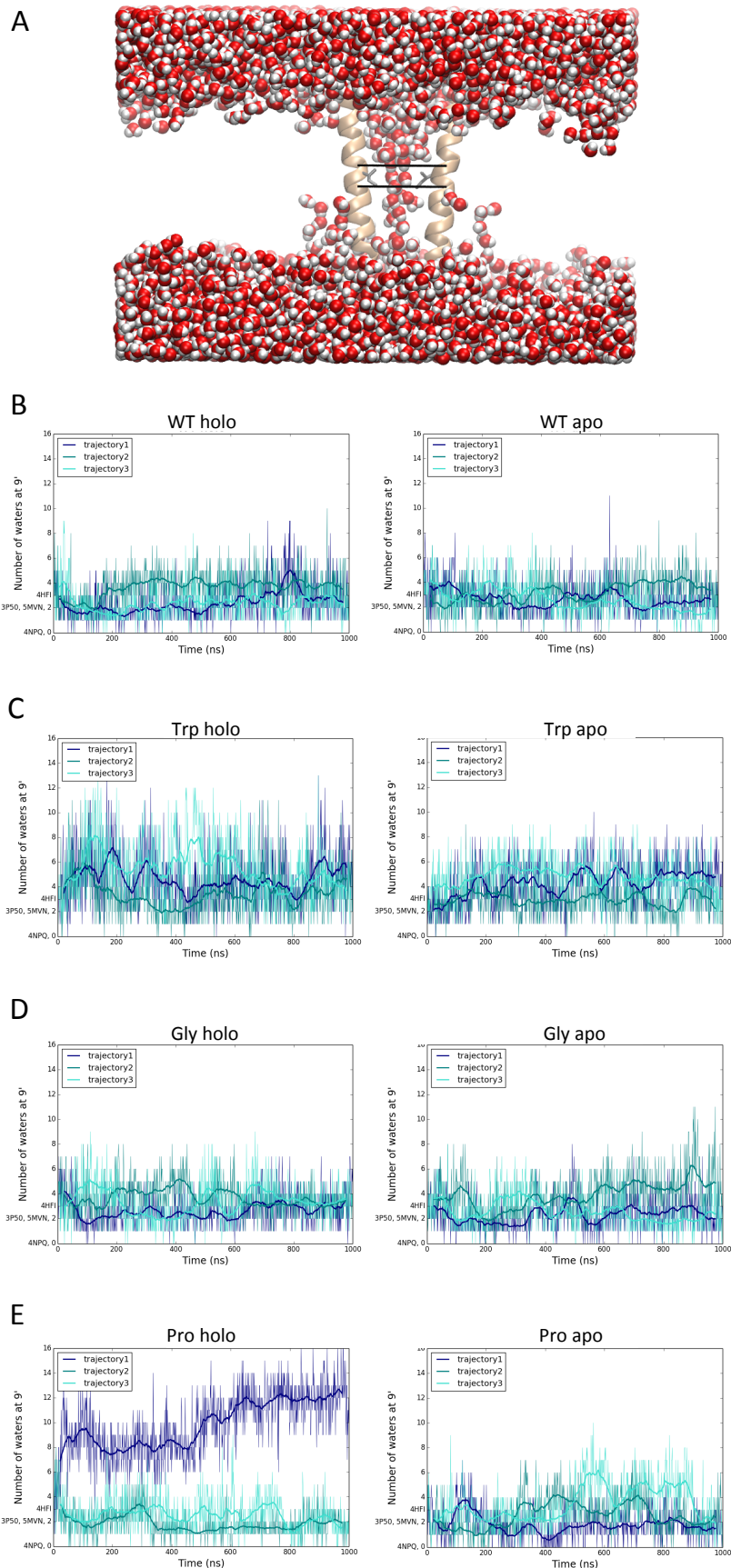
Fig. S3 Pore hydration at the hydrophobic gate. *(A)* Representative simulation frame showing water molecules and M2 helices of two GLIC subunits. The number of water molecules at the hydrophobic gate were quantified in the region between the two horizontal lines and plotted for each holo (*Left*) and apo (*Right*) simulation of *(B)* Met-205 (WT), *(C)* Trp-205, *(D)* Gly-205, and *(E)* Pro-205 variants. Water molecules at equivalent positions in equilibrated open (4HFI), closed (4NPQ) and holo WT (3P50) and Trp-variant (5MVN) are indicated on the y-axis.
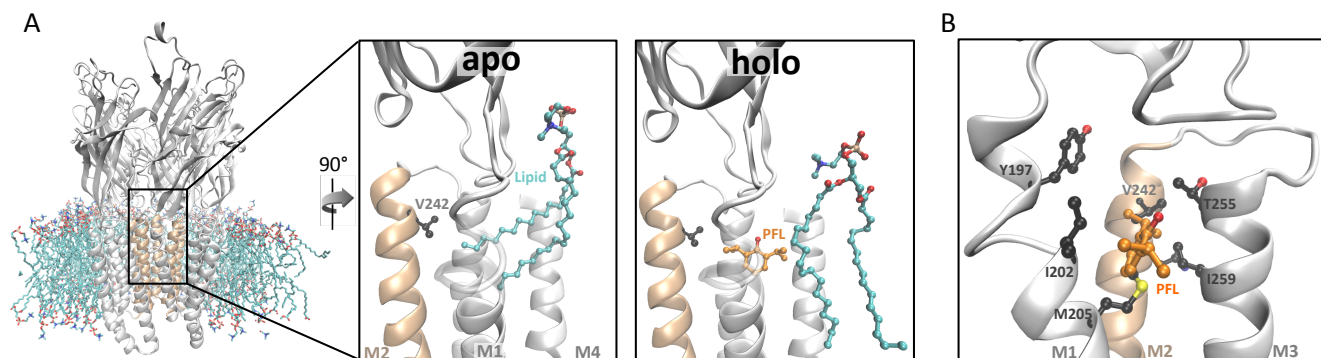
Fig. S4 Membrane-embedded protein setup for molecular dynamics simulations. *(A)* GLIC (gray) embedded in POPC lipids (turquoise). Pore-lining M2 helices are colored in tan. *Inset:* 90°-rotated zoom views of representative PFL binding sites. In apo simulations (*Left*), lipid molecules have access to the intrasubunit cavity; in holo simulations (*Right*), the cavity is primarily occupied by PFL (orange). *(B)* Side view of the intrasubunit PFL-binding site, with lipids and helix M4 removed to reveal PFL (orange) and cavity-defining residues 197, 202 and 205 in M1; 242 in M2; and 255 and 259 in M3 (black). Propofol, lipids and explicit amino acid side chains are colored by heteroatom (blue, N; red, O; yellow, S).
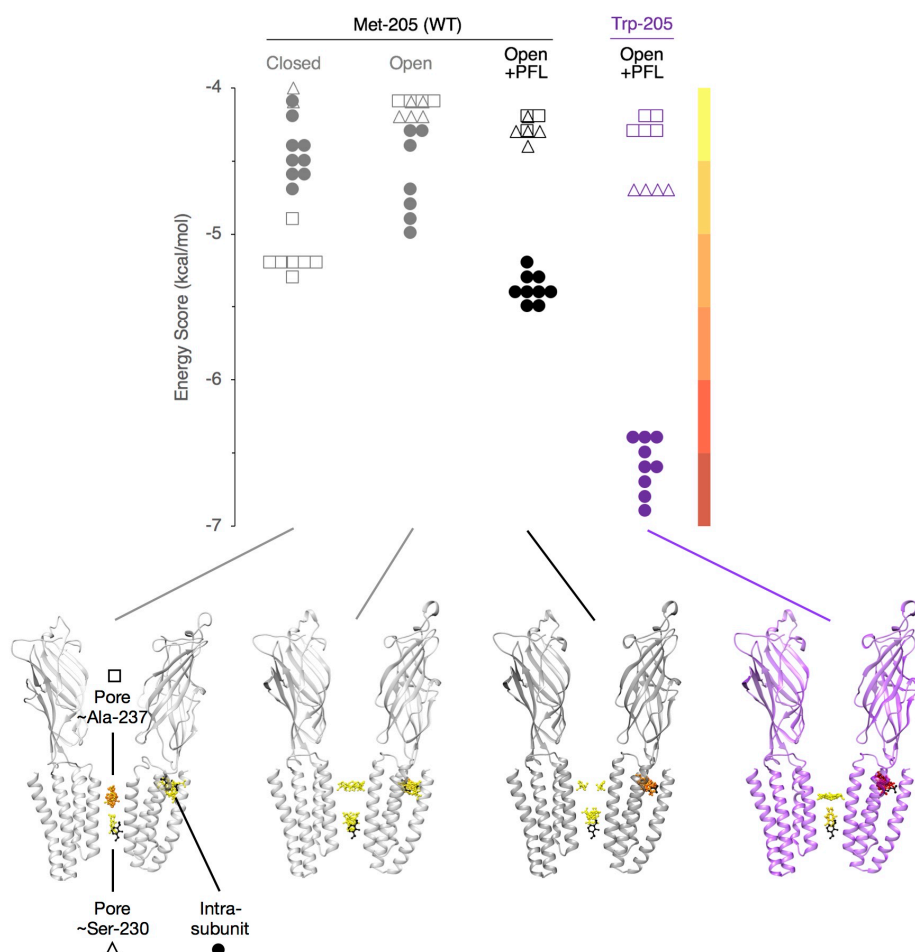

Fig. S5 Computational docking to intrasubunit and pore sites in GLIC experimental structures. *Top,* nine most favorable energy score clusters determined in AutoDock Vina for apo closed (PDB ID 4NPQ, gray) and open (4HFI, gray), and holo open WT (3P50, black) and Trp-205 (5MVN, purple), X-ray structures, using search volumes enclosing the intrasubunit binding cavity (filled symbols) or the channel pore (open symbols). Binding poses in the channel pore are classified by proximity to residue Ser-230 (triangles) or Ala-237 (squares). *Bottom,* representative docking poses for each cluster, colored according to scale bar at right, from most (dark red) to least favorable (yellow) binding energy scores. For comparison, crystallographic positions of PFL in the open-state intrasubunit site (3P50) and closed channel pore (5MUO) are shown in black.
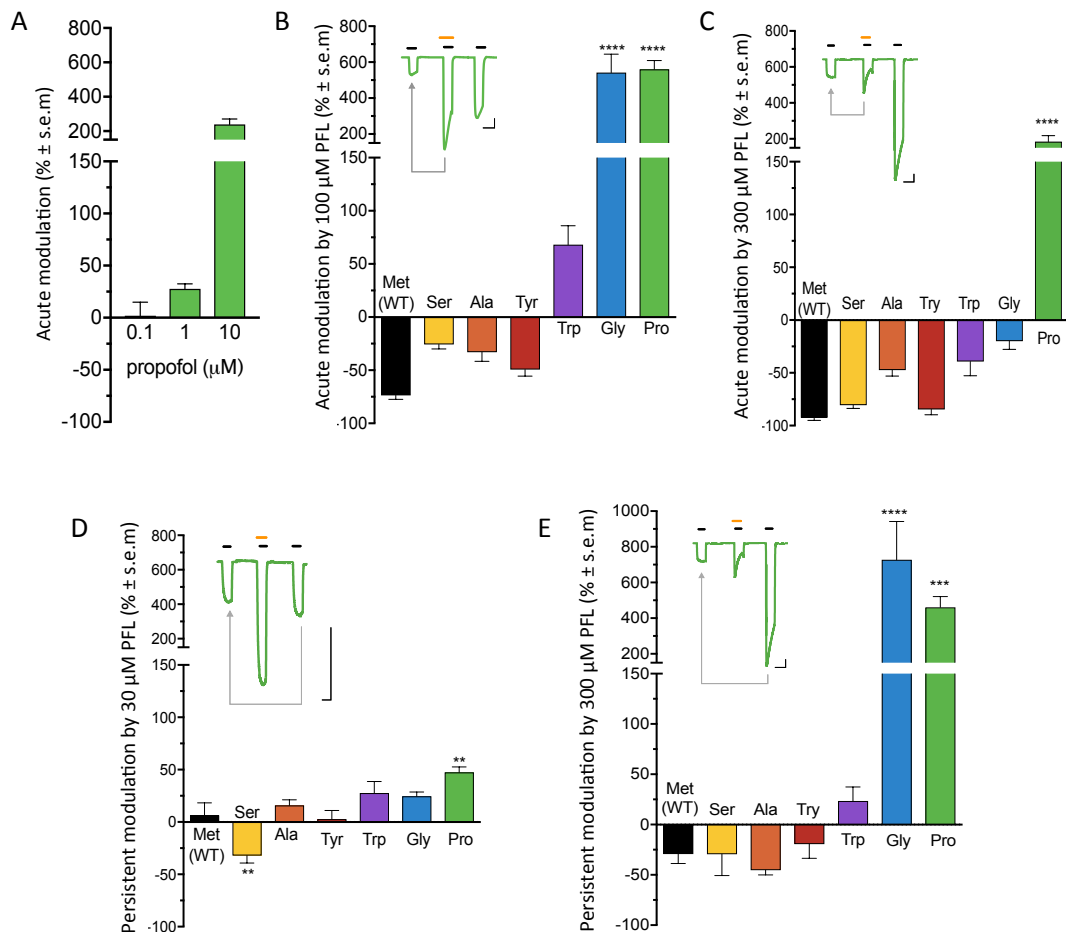
Fig. S6 Acute and persistent modulation of GLIC M1-205 variants. (A) Acute modulation of GLIC Pro-205 by lower PFL concentrations, calculated as % change in co- vs. pretreatment currents (as in Fig. 2*F*). **(B)** Acute modulation of GLIC M1-205 variants by 100 μM PFL, calculated as in *A*. **(C)** Acute modulation by 300 μM PFL, analyzed as in *A*. **(D)** Persistent modulation by 30 μM PFL, calculated as % change in post- vs. pretreatment currents (as in Fig. 3*C*). **(E)** Persistent modulation by 300 μM PFL, analyzed as in *D*. In all panels, significance is relative to WT, determined by one-way analysis of variance, $n = 4$–11 (**$P < 0.01$, ***$P < 0.001$, ****$P < 0.0001$). In *B–E*, insets show sample traces for GLIC Pro-205, with arrow indicating comparison in corresponding graphs; scale bars, 1 μA

Activation dependence of PFL washout. Sample traces show M-PFL, then posttreatment repeated 2–6 times. **(B)** Time w pretreatment activation, then treatment with 100 μM PFL tion. In *A–B*, scale bars represent 1 μA vs 2 min. **(C)** Time rol 6-min treatment of WT, calculated as % change in post- relative to 0-min exposure, determined by one-way analysis of variance, $n = 4$–6 (*$P < 0.05$, ****$P < 0.0001$).

9

Fig. S8 Acute and persistent modulation of GLIC M1-205 variants by bromoform and ethanol. *(A)* Acute modulation by 600 mM ethanol, calculated (as in Fig. 2*F*) as % change in co- vs. pretreatment currents. *(B)* Acute modulation by 1 mM bromoform, calculated as in *A*. *(C)* Persistent modulation by 600 mM ethanol, calculated (as in Fig. 3*C*) as % change in post- vs. pretreatment currents. *(D)* Persistent modulation by 1 mM bromoform, calculated as in *C*. In all panels, significance is relative to WT, determined by one-way analysis of variance, $n = 4$–11 (*$P < 0.05$, **$P < 0.01$, ****$P < 0.0001$). Insets show sample traces for GLIC Pro-205, arrow indicating comparison in corresponding graphs; scale bars 1 μA vs. 2 min.
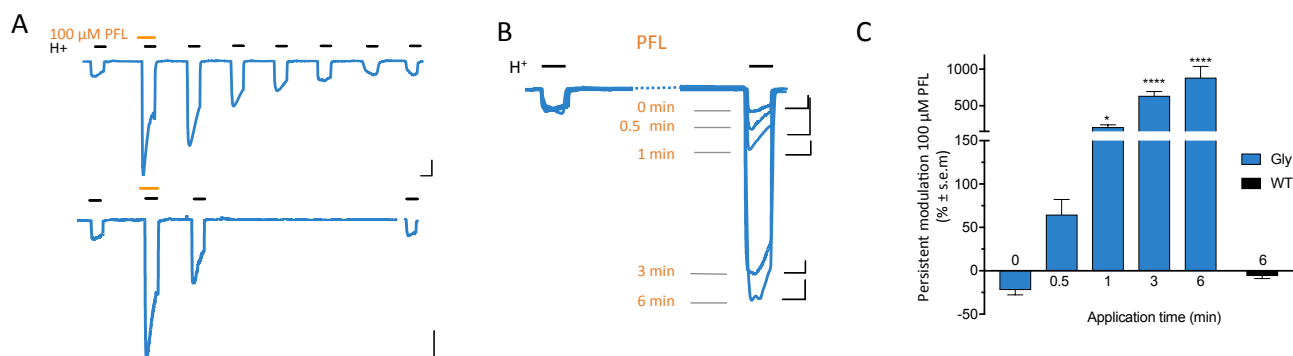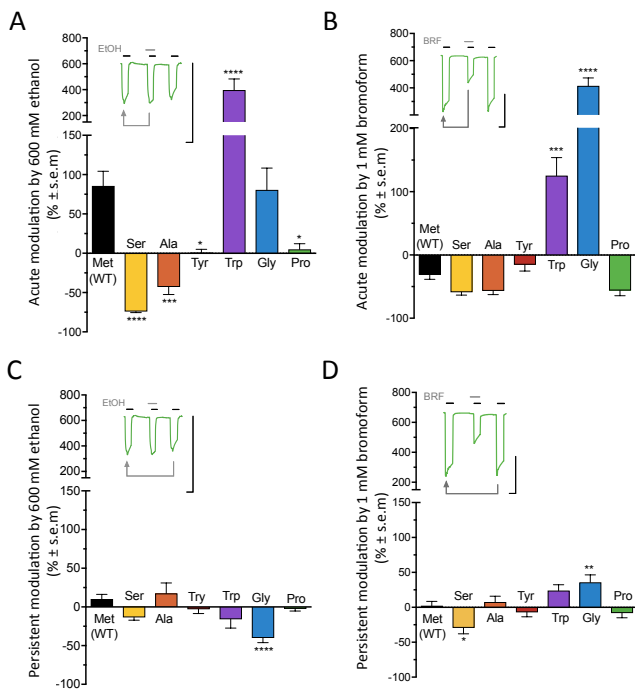

Fig. S9 Model for differential modulation at lower PFL concentrations. (A) Overlaid sample traces for GLIC WT (black) and Pro-205 (green) as in Fig. 2*E*, showing EC_{10} activation pretreatment (Left), cotreatment with 30 μM PFL (*Center*), and posttreatment (*Right*). **(B)** In the absence of PFL (*Left*), intrasubunit cavities in WT GLIC (Met-205) are largely contracted. Therefore, binding of PFL to the pore is favored over the intrasubunit site, leading to inhibition. Only a small amount of PFL diffuses into the membrane and almost all of it is expected to wash out (*Right*). **(C)** In Pro-205 and related variants, intrasubunit cavities are relatively deep even in the absence of PFL (*Left*). Upon cotreatment (*Center*), PFL can bind with little cavity expansion, producing potentiation that is partly compensated by inhibitory binding in the pore. After washout (*Right*), almost no PFL is left in the system; therefore no significant effects are expected. In panels *B*–*C,* three subunits of GLIC are represented as in Fig. 1*A*.

10

```
              M1→                        M2→                              M3→
Glycine α1   ERQMGYYLIQMYIPSLLIVILSWISFWINMDAAPARVGLGITTVLTMTTQSSGSRASLPKVSYVK-AIDIWMAVCLLFVFSALLEYAAVNFVSRQHKE
Glycine β    RRQVGFYMMGVYAPTLLIVVLSWLSFWINPDASAARVPLGIFSVLSLASECTTLAAELPKVSYVK-ALDVWLIACLLFGFASLVEYAVVQVMLNNPKR
GABAA α1     KRKIGYFVIQTYLPCIMTVILSQVSFWLNRESVPARTVFGVTTVLTMTTLSISARNSLPKVAYAT-AMDWFIAVCYAFVFSALIEFATVNYFTKRGYA
GABAA β3     KRNIGYFILQTYMPSILITILSWVSFWINYDASAARVALGITTVLTMTTINTHLRETLPKIPYVK-AIDMYLMGCFVFVFLALLEYAFVNYIFFGRGP
GABAA γ2     SRRMGYFTIQTYIPCTLIVVLSWVSFWINKDAVPARTSLGITTVLTMTTLSTIARKSLPKVSYVT-AMDLFVSVCFIFVFSALVEYGTLHYFVSNRKP
- - - - - - - - - - - - - - - - - - - - - - - - - - - - - - - - - - - - - - - - - - - - - - - - - - - - -
GABAA ρ1     RRHIFFFLLQTYFPATLMVMLSWVSFWIDRRAVPARVPLGITTVLTMSTIITGVNASMPRVSYIK-AVDIYLWVSFVFVFLSVLEYAAVNYLTTVQER
nACh α4      RRLPLFYTINLIIPCLLISCLTVLVFYLPSE-CGEKITLCISVLLSLTVFLLLITEIIPSTSLVIPLIGEYLLFTMIFVTLSIVITVFVLNVHHRSPR
nACh β2      RRKPLFYTINLIIPCVLITSLAILVFYLPSD-CGEKMTLCISVLLALTVFLLLISKIVPPTSLDVPLVGKYLMFTMVLVTFSIVTSVCVLNVHHRSPT
5-HT3A       RRRPLFYVVSLLLLPSIFLMVMDIVGFYLPPN-SGERVSFKITLLLGYSVFLIIVSDTLPATAIGTPLIGVYFVVCMALLVISLAETIFIVRLVHKQDL
5-HT3B       RRHPLVYVVSLLIPSIFLMLVDLGSFYLPPN-CRARIVFKTSVLVGYTVFRVNMSNQVPRSVGSTPLIGHFFTICMAFLVLSLAKSIVLVKFLHDEQR
GLIC         SRQYFSYIPNIILPMLFILFISWTAFWSTS--YEANVTLVVSTLIAHIAFNILVETNLPKTPYMT-YTGAIIFMIYLFYFVAVIEVTVQHYLKVESQP
              197    202 205                               239 242        255   259
```
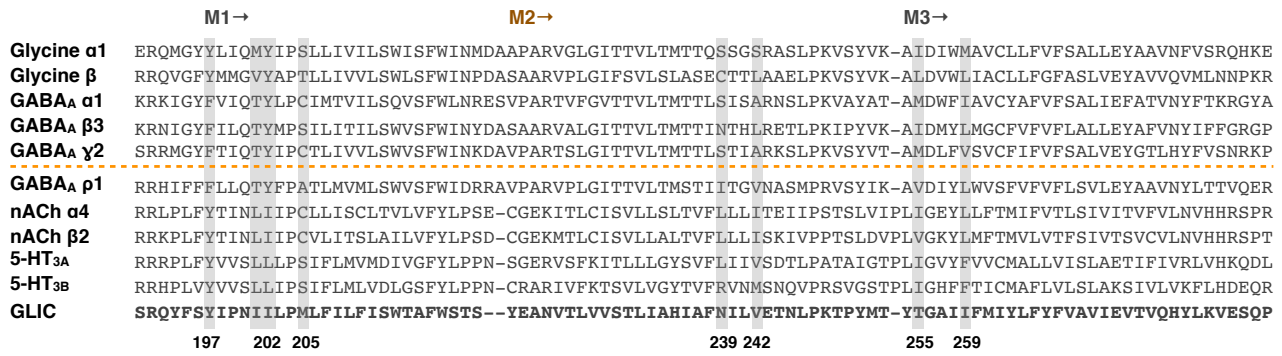
Fig. S10 Sequence alignment of GLIC transmembrane helices M1–M3 and equivalent regions of representative human pLGICs, with residues lining the intrasubunit PFL cavity highlighted in gray. Sequences above and below the dotted line are primarily associated with general anesthetic potentiation and inhibition, respectively.

SI REFERENCES

1. Lindorff-Larsen K*, et al.* (2010) Improved side-chain torsion potentials for the Amber ff99SB protein force field. *Proteins* 78(8):1950-1958.
2. Kasson PM, Lindahl E, & Pande VS (2010) Atomic-resolution simulations predict a transition state for vesicle fusion defined by contact of a few lipid tails. *PLoS Comput Biol* 6(6):e1000829.
3. Berger O, Edholm O, & Jahnig F (1997) Molecular dynamics simulations of a fluid bilayer of dipalmitoylphosphatidylcholine at full hydration, constant pressure, and constant temperature. *Biophys J* 72(5):2002-2013.
4. Nury H*, et al.* (2011) X-ray structures of general anaesthetics bound to a pentameric ligand-gated ion channel. *Nature* 469(7330):428-431.
5. Jorgensen WL, Chandrasekhar J, Madura JD, Impey RW, & Klein ML (1983) Comparison of simple potential functions for simulating liquid water. *J Chem Phys* 79(2):926-935.
6. Lundborg M & Lindahl E (2015) Automatic GROMACS topology generation and comparisons of force fields for solvation free energy calculations. *J Phys Chem B* 119(3):810-823.
7. Sousa da Silva AW & Vranken WF (2012) ACPYPE - AnteChamber PYthon Parser interfacE. *BMC Res Notes* 5:367.
8. Wang J, Wang W, Kollman PA, & Case DA (2006) Automatic atom type and bond type perception in molecular mechanical calculations. *J Mol Graph Model* 25(2):247-260.
9. Wang J, Wolf RM, Caldwell JW, Kollman PA, & Case DA (2004) Development and testing of a general amber force field. *J Comput Chem* 25(9):1157-1174.
10. Abraham MJ*, et al.* (2015) GROMACS: High performance molecular simulations through multi-level parallelism from laptops to supercomputers. *SoftwareX* 1–2:19-25.
11. Berendsen HJC, van der Spoel D, & van Drunen R (1995) GROMACS: A message-passing parallel molecular dynamics implementation. *Comput Phys Commun* 91(1):43-56.
12. Van Der Spoel D*, et al.* (2005) GROMACS: fast, flexible, and free. *J Comput Chem* 26(16):1701-1718.
13. Bussi G, Donadio D, & Parrinello M (2007) Canonical sampling through velocity rescaling. *J Chem Phys* 126(1): 014101
14. Berendsen HJC, Postma JPM, Vangunsteren WF, Dinola A, & Haak JR (1984) Molecular-Dynamics with Coupling to an External Bath. *J Chem Phys* 81(8):3684-3690.
15. Hess B, Bekker H, Berendsen HJC, & Fraaije JGEM (1997) LINCS: A linear constraint solver for molecular simulations. *J Comput Chem* 18(12):1463-1472.
16. Parrinello M & Rahman A (1980) Crystal-Structure and Pair Potentials - a Molecular-Dynamics Study. *Phys Rev Lett* 45(14):1196-1199.
17. Schmidtke P, Bidon-Chanal A, Luque FJ, & Barril X (2011) MDpocket: open-source cavity detection and characterization on molecular dynamics trajectories. *Bioinformatics* 27(23):3276-3285.
18. Humphrey W, Dalke A, & Schulten K (1996) VMD: Visual molecular dynamics. *J Mol Graph Model* 14(1):33-38.
19. Hess B (2002) Determining the shear viscosity of model liquids from molecular dynamics simulations. *J Chem Phys* 116(1):209-217.
20. Trott O & Olson AJ (2010) Software News and Update AutoDock Vina: Improving the Speed and Accuracy of Docking with a New Scoring Function, Efficient Optimization, and Multithreading. *J Comput Chem* 31(2):455-461.
21. Pettersen EF*, et al.* (2004) UCSF chimera - A visualization system for exploratory research and analysis. *J Comput Chem* 25(13):1605-1612.
22. Fourati Z*, et al.* (2018) Structural basis for a bimodal allosteric mechanism of general anesthetic modulation in pentameric ligand-gated ion channels. *Cell Rep* 23(4):993-1004.
23. Heusser SA*, et al.* (2013) Functional validation of virtual screening for novel agents with general anesthetic action at ligand-gated ion channels. *Mol Pharmacol* 84(5):670-678.